Nuclear Engineering and Technology 53 (2021) 2341–2347

Contents lists available at ScienceDirect

Nuclear Engineering and Technology

journal homepage: www.elsevier.com/locate/net

Original Article

Improvement of signal and noise performance using single image super-resolution based on deep learning in single photon-emission computed tomography imaging system

Kyuseok Kim [a], Youngjin Lee [b, *]

[a] Department of Intergrative Medicine, Major in Digital Healthcare, Yonsei University, Seoul, Republic of Korea
[b] Department of Radiological Science, Gachon University, 191, Hambakmoero, Yeonsu-gu, Incheon, Republic of Korea

ARTICLE INFO

Article history:
Received 23 October 2020
Received in revised form
12 November 2020
Accepted 9 January 2021
Available online 23 January 2021

Keywords:
Nuclear medicine imaging
Single photon emission computed tomography
Super-resolution
Deep learning
Deep convolutional neural network
Quantitative evaluation of image quality

ABSTRACT

Because single-photon emission computed tomography (SPECT) is one of the widely used nuclear medicine imaging systems, it is extremely important to acquire high-quality images for diagnosis. In this study, we designed a super-resolution (SR) technique using dense block-based deep convolutional neural network (CNN) and evaluated the algorithm on real SPECT phantom images. To acquire the phantom images, a real SPECT system using a ^{99m}Tc source and two physical phantoms was used. To confirm the image quality, the noise properties and visual quality metric evaluation parameters were calculated. The results demonstrate that our proposed method delivers a more valid SR improvement by using dense block-based deep CNNs as compared to conventional reconstruction techniques. In particular, when the proposed method was used, the quantitative performance was improved from 1.2 to 5.0 times compared to the result of using the conventional iterative reconstruction. Here, we confirmed the effects on the image quality of the resulting SR image, and our proposed technique was shown to be effective for nuclear medicine imaging.

1. Introduction

Representative devices for nuclear medicine imaging include a gamma camera and single photon emission computed tomography (SPECT) that can acquire images from one or more directions using a single photon-emitting nuclide, as well as positron emission tomography (PET), which uses a positron-emitting nuclide with a relatively short half-life [1,2]. Fusion imaging devices such as PET/computed tomography (CT), PET/magnetic resonance imaging (MRI), SPECT/CT, and SPECT/MRI, which can simultaneously acquire functional and anatomical images, have recently been developed and are actively being used [3–7].

Images acquired using a single photon-based nuclear medicine device have a crucial problem of a low spatial resolution and high noise level owing to a low photon counting in the detector [8,9]. As a result of comparing the imaging performances of nuclear medicine devices, Jansen et al. reported that the sensitivity of clinical PET and SPECT was ~3% and ~0.03%, respectively, and that the spatial resolution was ~5 and ~10 mm [8]. In particular, because nuclear medicine images use a significantly lower number of photons than images using X-rays, a relatively high amount of noise is observed. To remove such noise, a large number of radiopharmaceuticals are used or a method for increasing the examination time is applied; however, a large problem occurs in that the exposure dose of the patient increases [10,11]. Because radiopharmaceuticals used for examination have a physical half-life as radioactive isotopes and a biological half-life when injected into the human body, the total examination time cannot be extended indefinitely. In addition, in accordance with the recommendations of the International Commission on Radiological Protection, the proposed human exposure dose to achieve an optimized defense is kept as low as possible.

Another method to improve the quality of nuclear medicine images is to develop a new detector material with an excellent performance. According to Lecoq, a scintillation type detector using alkali-halide, oxide compounds, and pulling-down technology as new nuclear medicine detector materials has been proposed [12]. In particular, research on the development of a detector using room-temperature semiconductor materials such as cadmium zinc telluride (CZT) or cadmium telluride (CdTe) has been actively

* Corresponding author. Department of Radiological Science, Gachon University, Republic of Korea.
E-mail address: yj20@gachon.ac.kr (Y. Lee).

https://doi.org/10.1016/j.net.2021.01.011

conducted [13–15]. In a study by Lee et al. it was confirmed that the spatial resolution and sensitivity characteristics were improved by 3.8- and 1.5-fold, respectively, compared to a general NaI(Tl) scintillation detector when using a CdTe material-based detector in nuclear medicine phantom images [13].

However, a relatively high cost is required to develop a detector with good performance for nuclear medicine imaging. In addition, photon-counting detector systems based on materials such as CZT or CdTe have difficulties in maintaining their cooling. In addition, the design of a highly efficient application-specific integrated circuit is difficult to achieve, and a high computing power is needed. The most useful method to improve the characteristics of a nuclear medicine image while overcoming these shortcomings is to use a software algorithm. The super-resolution (SR) technique is widely used in various imaging fields, and it has been announced that the overall image quality is improved when compared to a conventional algorithm [16–19].

The SR technique, which is the restoration of a high-resolution (HR) image from a low-resolution (LR) image, can be written using Eq. (1) [20–22]:

$$y = DBMx + n, \tag{1}$$

where y is the LR image that results from the HR image x, when applying the degradation matrices including the subsampling matrix D, blur matrix B, and geometric warp matrix M. In addition, n represents a noise component. The larger the upscaling factor is, the more highly ill-posed the problem is in recovering the details in the SR image. The methods used for SR can be classified as 1) multi-image-based SR and 2) example-based SR. Multi-image based SR is a classical technique and is a method for generating an unknown HR image by imposing a set of linear constraints over the LR images obtained by subpixel shifting [23,24]. However, it is difficult to expect high quality in a large upsampling and it has limitations in terms of dose because it requires several LR images [25,26]. Another approach is single image SR [27–29] using an example database consisting of LR and HR image pairs. This method estimates the HR image from the learned algorithm [30–34] and the example-based SR technique has overcome the limitations of the multiple existing SR techniques. Recent studies on SR [35–37] have achieved an outstanding performance with regard to preserving the high-frequency detailed information using varied deep convolutional neural network (CNN). However, this method incurs a problem of a vanishing gradient in a very deep CNN, and a skip connection is the most effective approach to help with the training because it alleviates the vanishing gradient. Moreover, the dense skip connection has demonstrated an improved performance by providing additional information at different layers. In particular, DenseNet [38] has been spotlighted for its SR results [39,40] owing to a concatenation using a dense skip connection.

In this study, we investigated the proposed framework to improve the SPECT image quality in terms of noise and resolution using DenseNet. The proposed method increases the amount of detected photons per unit area for reducing the effect on Poisson noise and improving the resolution through the SR process. We expected that overcoming inherent limitation such as unnatural result (i.e., cartoon-like representation) when using the existing noise reduction algorithm. We evaluated the image performance based on a visual assessment, contrast-to-noise ratio (CNR) [41], coefficient of variation (COV) [42], peak signal-to noise ratio (PSNR) [43], and normalized noise power spectrum (NNPS) [44] of two physical phantoms. In the following sections, we briefly describe the implementation of the experiment and discuss the results in detail.

2. Materials and methods

2.1. SPECT imaging system and phantoms used

As the radiation source, ^{99m}Tc at 2.2 mCi (500 kBq) was used along with a low-energy high-resolution (LEHR) parallel-hole collimator. This commercial SPECT system (Discovery NM/CT 670, GE Healthcare, USA) mainly consists of NaI(Tl) scintillation detectors with approximately 9.8% energy resolution and mechanical support for patient movement. The source-to-collimator distance was 18.5 cm. In addition, 120 projections were obtained at 30 s per image, and reconstructed images were restored in DICOM format with a 14-bit depth. To acquire nuclear medicine images, Hoffman brain and Jaszczak phantoms (spatial resolution) were used in this study. Fig. 1 shows our experimental setup, including the detector system and Hoffman brain phantom.

2.2. Proposed super-resolution (SR) process

Fig. 2 shows a simplified flowchart of the designed SR process using a dense block-based deep CNN applied to a SPECT image. Among the end-to-end deep-learning models, we employed an extremely deep CNN to predict the residual images and used the SRDenseNet_All architecture by Tong et al. [39]. This consists of a convolution layer to learn the low-level features, a DenseNet block section for learning the high-level features with a dense skip connection, a 1×1 convolution layer (bottleneck layer) to maintain compactness and reduce the computation cost, two 3×3 deconvolution layers with 256 feature maps for the upscaling filter, and 3×3 convolution layers (reconstruction layer) to generate the residual image of a single channel. Here, the DensNet block can be expressed by Eq. (2):

$$p_l = H_l([p_0, p_1, p_2, \ldots, p_{l-1}]), \tag{2}$$

where p_l is the data at the l^{th} layer and $H_l(\cdot)$ is a function that has been assembled through batch normalization [45], ReLu (activation layer), and 3×3 convolution layers. Here, $[p_0, p_1, p_2, \ldots, p_{l-1}]$ indicates that the concatenation gathered all of the feature maps until the $(l-1)^{th}$ layer. We designed 8 convolution layers and generated 128 feature maps in one DenseNet block. To recover the weights and bias, the cost function used the mean squared error (MSE) as follows:

$$\widehat{\theta} = \underset{\theta}{\operatorname{argming}}(\theta),$$

$$g(\theta) = \frac{1}{N} y - N(\theta|I)_2^2, \tag{3}$$

$$\widehat{y} = N(\widehat{\theta}|I),$$

where I is the input patch, y is the label patch, θ is the group of weights and biases in the network, and $N(\cdot)$ is the designed network. For optimization, the θ adoptive momentum estimation (Adam) optimizer [46] is used with an initial learning rate of 10^{-4} and is decreased by a factor of 10 when validation loss plateaus. A mini-batch size of 8 was set during the training, and the number of epochs was 150. The energy window was set to 20% and eight random patches were generated using the image augmentation.

A total of 500 reconstructed slices were acquired with a GE Healthcare machine as an LR (slice dimensions of $150 \times 150 \times 150$ voxels and pixel size of 5.6 mm)–HR (slice dimensions of $300 \times 300 \times 150$ voxels and pixel size of 2.8 mm) dataset pair. Here,

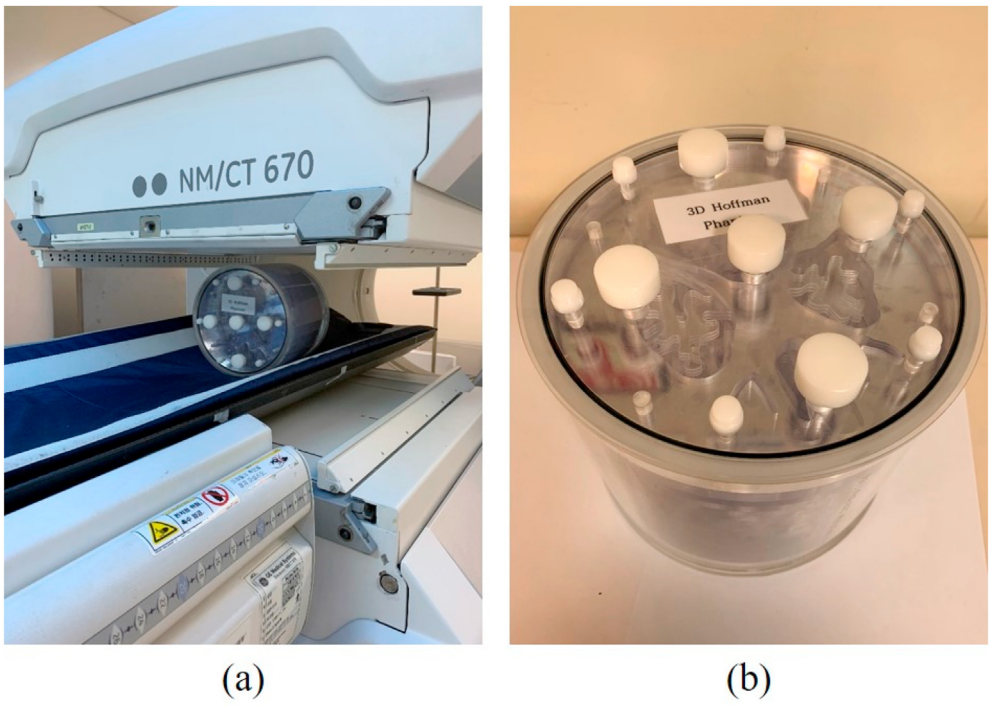

Fig. 1. Photographs of (a) actual experimental single photon emission computed tomography (SPECT) imaging system and (b) Hoffman brain phantom.

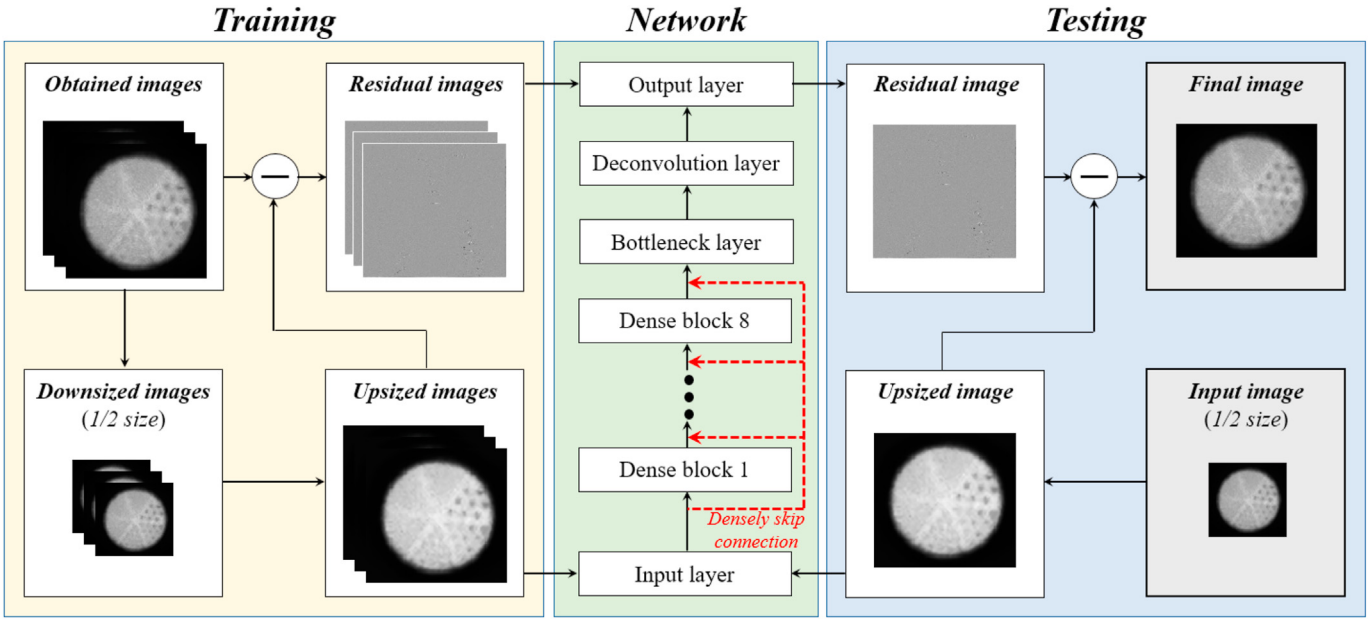

Fig. 2. Simplified flowchart of the designed super-resolution algorithm using dense block based deep convolutional neural network for SPECT image.

400 pairs of data are used as the training dataset and the rest of the data are used as the test set. We generated a residual image by subtracting between HR images and upsampled the LR images containing information about the degradation owing to the sub-sampling, blur, and geometric warp. The network was trained using a single GPU (GTX 1080Ti, 11 GB of memory, NVIDIA, USA) and Pytorch.

2.3. Quantitative evaluation of image quality

We evaluated the noise properties (e.g., CNR, COV, and NNPS) and visual quality metrics (e.g., PSNR) to confirm the ability of the designed SR algorithm in acquiring the SPECT images. The CNR, COV, NNPS, and PSNR were calculated as follows:

$$\mathrm{CNR} = \frac{\left|A_{\mathrm{Target}} - A_{\mathrm{Background}}\right|}{\sqrt{{\sigma_{\mathrm{Target}}}^2 + {\sigma_{\mathrm{Background}}}^2}}, \tag{3}$$

$$\mathrm{COV} = \frac{\sigma_T}{S_T}, \tag{4}$$

$$\mathrm{NNPS}(u,v) = \frac{\mathrm{NPS}(u,v)}{(\text{large area signal})^2}, \tag{5}$$

$$\mathrm{NPS}(u_n, v_k) = \lim_{N_x N_y, M \to \infty} \frac{\Delta x \Delta y}{M \cdot N_x N_y} \sum_{m=1}^{M} \left| \sum_{i=1}^{N_x} \sum_{j=1}^{N_y} \left(I\left(x_i, y_j\right) - S\left(x_i, y_j\right) \right) \times \right) \exp(-2\pi i (u_n x_i + v_k y_i)) \Big|^2$$

$$\mathrm{PSNR} = 20 \cdot \log_{10}\left(\frac{Max_f}{\sqrt{MSE}}\right) \tag{6}$$

where A_{Target} and σ_{Target} represent the mean and standard deviation of the target ROIs, respectively; $A_{Background}$ and $\sigma_{Background}$ represent the mean and standard deviation of the background ROIs, respectively; I is the image intensity; S is the average background intensity; N_x, N_y and $\Delta x, \Delta y$ account for the numbers of pixels and pixel sizes on the X- and Y-axes, respectively; and Max_f is the maximum signal value.

3. Results and discussion

Fig. 3 shows the experimental results of the 50th slice image using the Hoffman brain phantom for (a) a reconstructed image with filtered back-projection reconstruction (FBP), which is a conventional reconstruction technique, (b) a reconstructed image with an iterative reconstruction using OSEM under the conditions of 5 iterations and 10 subsets, (c) a residual image from the proposed framework, and (d) a reconstructed image using the proposed method when applying the reconstructed half-size image through the OSEM method. The enlarged image of Fig. 3 (d) shows that the object structure can be better identified, as compared to that of the enlarged image in Fig. 3 (b). Fig. 4 shows another example of a SPECT slice image using the Hoffman phantom and (a) the 65th slice image among the FBP reconstruction data (b) that of the OSEM reconstruction data, and (c) restored slice image using the proposed method from the OSEM slice image at half projection size. From the previous results of Fig. 3, it can be seen visually that the proposed image in Fig. 4 (c) has less noise while the structure of the object is distinguished, compared to that of the other two images. Here, the expressed regions of interest (ROIs) are applied for a quantitative evaluation using the CNR, COV, and PSNR. Fig. 5 shows the plots of the (a) CNR and (b) COV using ROI_1 and ROI_2 in Fig. 4 (a), and (c) the PSNR. The CNR values of the SR image, OSEM-based reconstructed image, and FBP-based reconstructed image were approximately 8.1, 7.6, and 2.7, respectively. The COV values of the proposed SR image, OSEM-based reconstructed image, and FBP-based reconstructed image were calculated to be approximately 1.02, 0.15, and 0.03, respectively. In addition, the PSNR factors of the three images were observed to be approximately 13.7, 39.4, and 47.8, respectively. It was confirmed quantitatively that the proposed algorithm performs quite effectively at improving the image quality.

Fig. 6 shows (a) the 50th slice image generated through a reconstruction using the ordered subset expectation maximization (OSEM) method, (b) an image denoised using the non-local means (NLM) algorithm applied to the slice image, and (c) an SR image

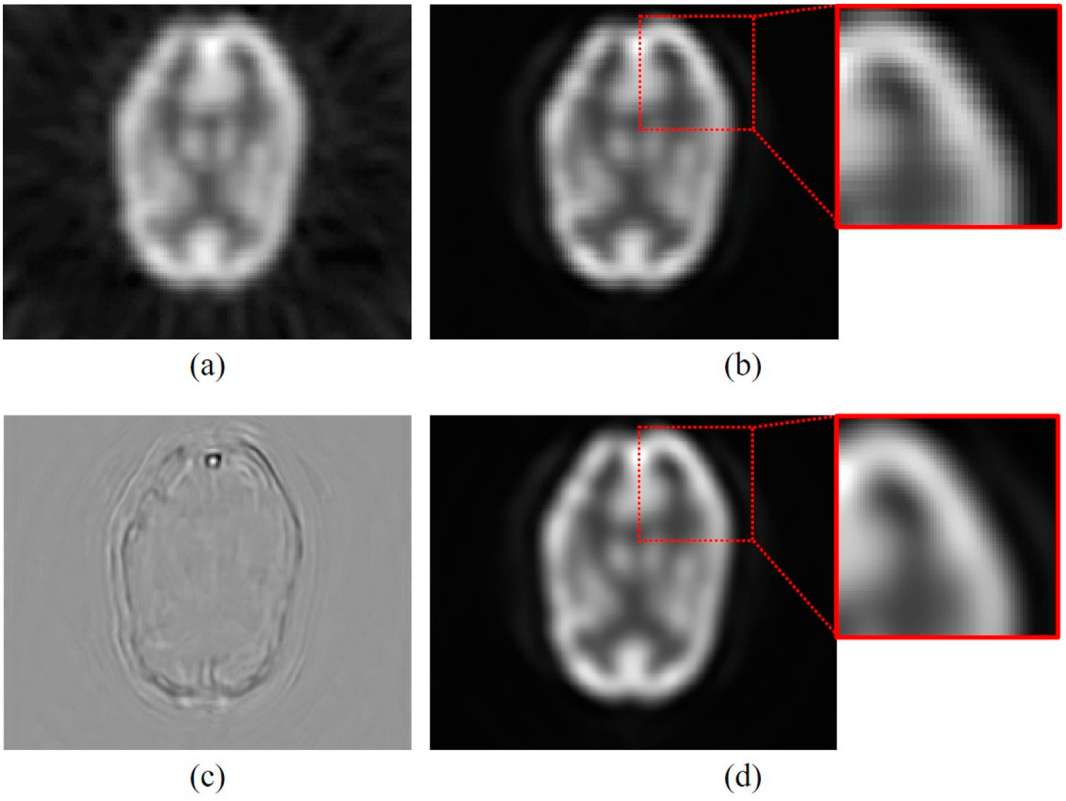

Fig. 3. Experiment results of 50th slice image using the Hoffman phantom for (a) reconstructed image with FBP, (b) reconstructed image with iterative reconstruction with OSEM using 5 iterations and 10 subsets, (c) residual image from deep-learning network, and (d) image reconstructed using the proposed method when applying a reconstructed half-size slice image with the OSEM method.

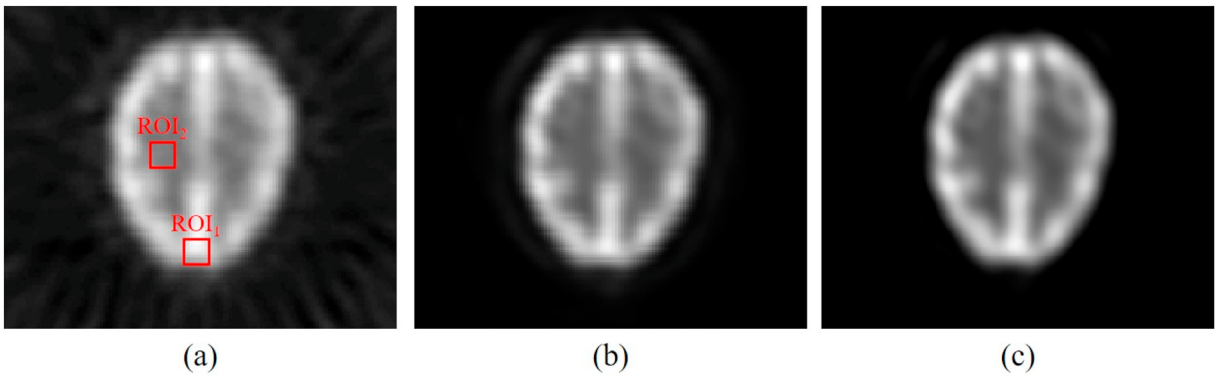

Fig. 4. Examples of 65th slice image obtained using the Hoffman phantom when applying (a) the FBP reconstruction data (b) OSEM reconstruction data, and (c) the proposed method with the OSEM slice image at half the projection size.

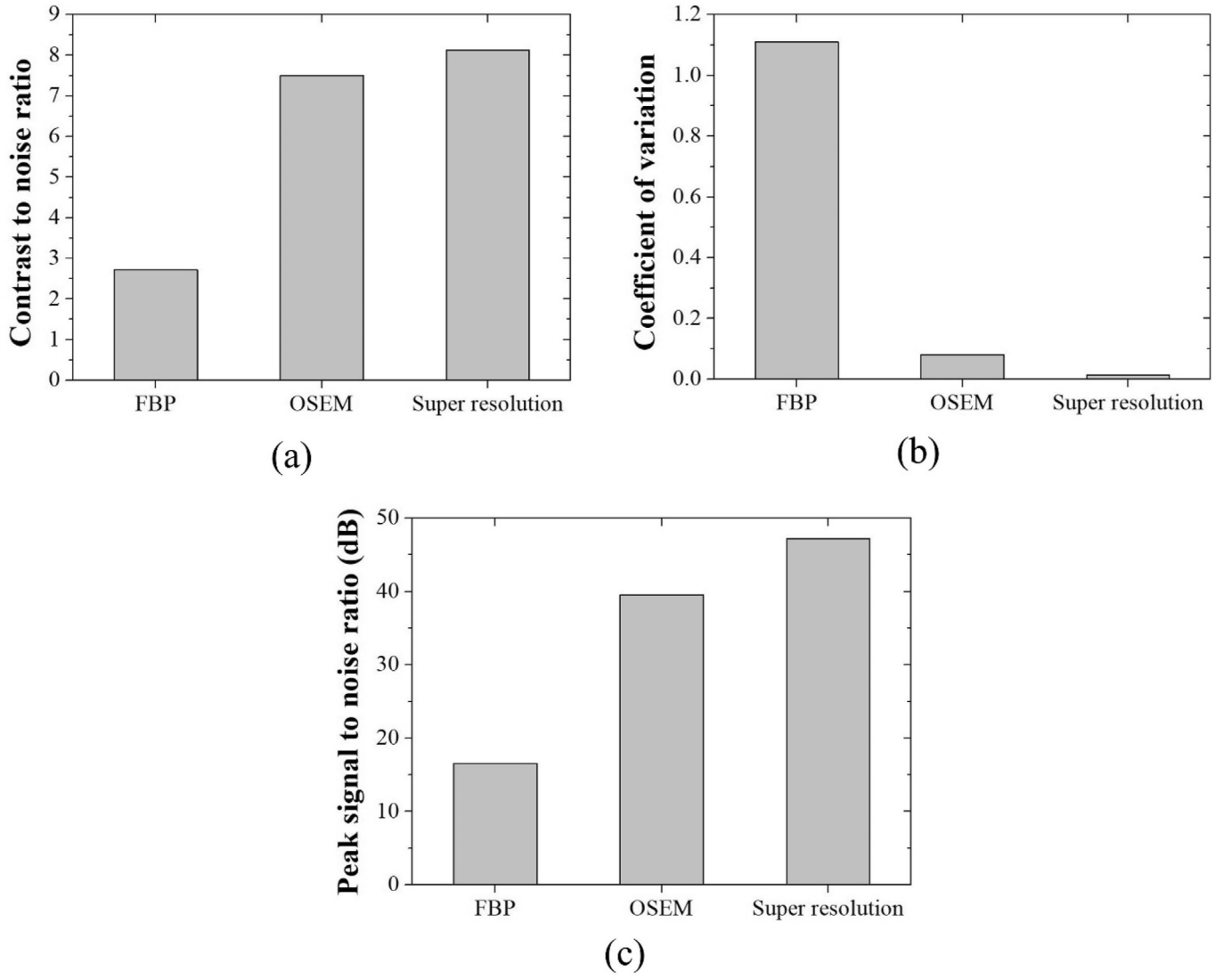

Fig. 5. Plots of (a) CNR, (b) COV using ROIs 1 and 2 in Fig. 4 (a), and (c) PSNR.

achieved using the proposed framework from the OSEM-based reconstructed slice image at half size as compared to that of the slice image from (a). Here, the NLM algorithm showed the improved image quality in a SPECT image [47] and we compared between applied image with NLM algorithm and proposed method. The NLM algorithm is computed as follows:

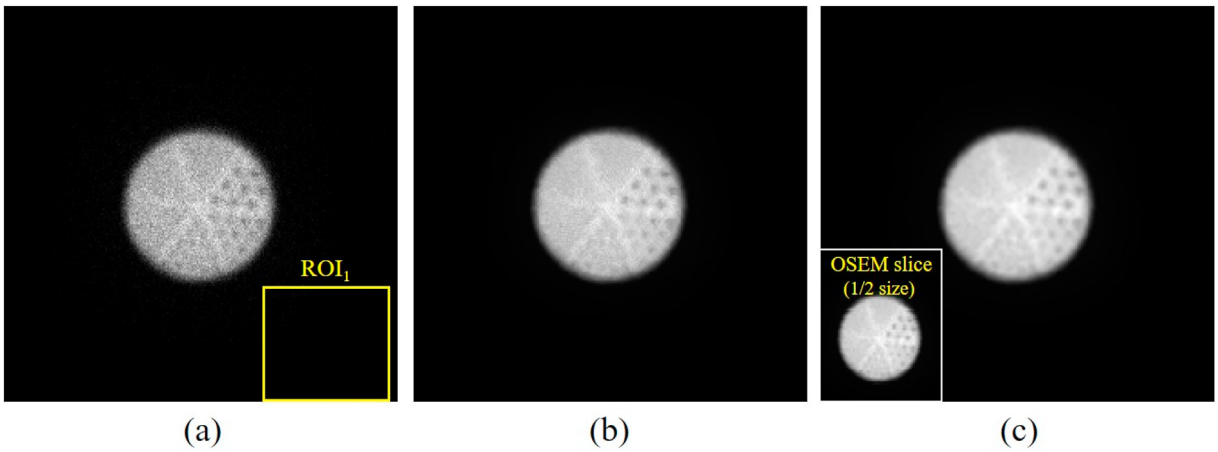

Fig. 6. (a) SPECT image slice of Jaszczak phantom using the iterative reconstruction with OSEM, (b) denoised slice image with OSEM-based reconstructed slice, and (c) proposed SR image using the half-sized OSEM-based reconstructed slice.

$$p(s) = \sum_{t \in \Omega_s} \frac{w_f(s,t)}{\sum_{t' \in \Omega_s} w_f(s,t')} f(s), \tag{7}$$

$$w_f(s,t) = exp\left(-\frac{t^2}{2N_f \sigma_f^2} \right),$$

where f is degraded image with coordinate (s, t), Ω_s is the search neighborhood in entire domain, N_f is the number of image, σ_f is the proportional expected parameter which is depends on the patches at the center pixels s and t. The image quality of Fig. 6 (c) shows an improved noise property while distinguishing the macrostructure of the holes. As the figure indicates, the proposed framework operates well for the SR in a SPECT image. For a quantitative evaluation used to characterize the noise, Fig. 7 shows the 1D NNPS calculated using the ROI_1 box shown in Fig. 6 (a). Here, the 1D NNPS of the proposed image at all spatial frequencies was improved compared to that of the other slices.

In applying the proposed method, we considered that it is difficult to distinguish the object if the resolution of the reconstructed image at half size is lower than the minimum resolution required for the object to be observed. However, these results indicate that the proposed method using the SR approach after obtaining an image with noise characteristics improved through a physical method is extremely effective in terms of the image performance of the resolution and noise when compared to that of an image restoration method applied through a denoising technique. Therefore, the proposed method is expected to be utilized to obtain a better image performance with regard to the price of the equipment and the exposure time of the radioisotope.

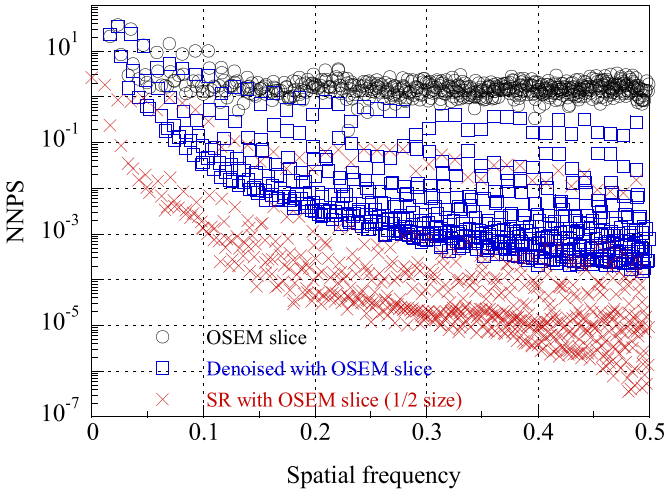

Fig. 7. The 1D NNPS calculated using ROI_1 box in Fig. 6 (a). The NNPS characteristics of the proposed image at all spatial frequencies were improved, compared to those of the other slices.

4. Conclusion

We investigated the proposed framework for improving signal and noise performane using the SR technique in the nuclear medicine SPECT images. We performed the experiment to evaluate the effectiveness of the propose method using two physical phantoms. The proposed images showed improved quantitative values including the CNR, COV, and PSNR metrics, compared to those of OSEM and FBP based reconstructed images. Moreover, the 1D NNPS of the proposed image at all spatial frequencies was improved compared to that of the denoised image from OSEM based reconstructed image. Consequently, it was demonstrated that the proposed algorithm can achieve an excellent imaging performance by producing a high spatial resolution and lower image noise. Thus, the proposed image restoration framework appears to be effective for improving image quality in SPECT as well as in conventional nuclear medicine imaging system.

Declaration of competing interest

The authors declare that they have no known competing financial interests or personal relationships that could have appeared to influence the work reported in this paper.

Acknowledgments

We would like to thank Prof. Chan Rok Park for helping us acquire the phantom data.

References

[1] K. Kim, M.H. Lee, Y. Lee, Investigation of a blind-deconvolution framework after noise reduction using a gamma camera in nuclear medicine imaging, Nuclear Engineering and Technology 52 (2020) 2594–2600.
[2] P. Zanzonico, Principles of nuclear medicine imaging: planar, SPECT, PET,

multi-modality, and autoradiography systems, Radiat. Res. 177 (2012) 349–364.
[3] Z.H. Cho, Y.D. Son, H.K. Kim, K.N. Kim, S.H. Oh, J.Y. Han, I.K. Hong, Y.B. Kim, A fusion PET–MRI system with a high-resolution research tomograph-PET and ultra-high field 7.0 T-MRI for the molecular-genetic imaging of the brain, Proteomics 8 (2008) 1302–1323.
[4] S. Sohn, H.J. Shi, S.H. Wang, S.K. Lee, S.Y. Park, J.S. Lee, J.S. Eom, Mycobacterium avium complex infection-related immune reconstitution inflammatory syndrome mimicking lymphoma in an human immunodeficiency virus-infected patient, Infection & Chemotherapy 50 (2018) 350–356.
[5] C.R. Park, Y. Lee, Comparison of PET image quality using simultaneous PET/MR by attenuation correction with various MR pulse sequences, Nuclear Engineering and Technology 51 (2019) 1610–1615.
[6] D.W. Townsend, Multimodality imaging of structure and function, Phys. Med. Biol. 53 (2008) R1–R39.
[7] C.T. Yang, K.K. Ghosh, P. Padmanabhan, O. Langer, J. Liu, D.N.C. Eng, C. Halldin, B. Gulyas, PET-MR and SPECT-MR multimodality probes: development and challenges, Theranostics 8 (2018) 6210–6232.
[8] F.P. Jansen, J.L. Vanderheyden, The future of SPECT in a time of PET, Nucl. Med. Biol. 34 (2007) 733–735.
[9] D.J. Rowland, S.R. Cherry, Small-animal preclinical nuclear medicine instrumentation and methodology, Semin. Nucl. Med. 38 (2008) 209–222.
[10] H.H. Li, J.R. Votaw, Optimization of PET activation studies based on the SNR measured in the 3-D hoffman brain phantom, IEEE Trans. Med. Imag. 17 (1998) 596–605.
[11] D.W. Townsend, Positron emission tomography/computed tomography, Semin. Nucl. Med. 38 (2008) 152–166.
[12] P. Lecoq, Development of new scintillators for medical applications, Nucl. Instrum. Methods Phys. Res. 809 (2016) 130–139.
[13] Y.J. Lee, S.J. Park, S.W. Lee, D.H. Kim, Y.S. Kim, H.J. Kim, Comparison of photon counting and conventional scintillation detectors in a pinhole SPECT system for small animal imaging: Monte Carlo simulation studies, J. Kor. Phys. Soc. 62 (2013) 1317–1322.
[14] S. Abbaspour, B. Mahmoudian, J.P. Islamian, Cadmium telluride semiconductor detector for improved spatial and energy resolution radioisotopic imaging, World J. Nucl. Med. 16 (2017) 101–107.
[15] P. Russo, F.D. Lillo, V. Corvino, P.M. Frallicciardi, A. Sarno, G. Mettivier, CdTe compact gamma camera for coded aperture imaging in radioguided surgery, Phys. Med. 69 (2020) 223–232.
[16] S. Pujals, N. Feiner-Gracia, P. Delcanale, I. Voets, L. Albertazzi, Super- resolution microscopy as a powerful tool to study complex synthetic materials, Nature Reviews Chemistry 3 (2019) 68–84.
[17] D. Ravi, A.B. Szczotka, S.P. Pereira, T. Vercauteren, Adversarial training with cycle consistency for unsupervised super-resolution in endomicroscopy, Med. Image Anal. 53 (2019) 123–131.
[18] T. Mamyrbayev, K. Ikematsu, P. Meyer, A. Ershov, A. Momose, J. Mohr, Super-resolution scanning transmission X-ray imaging using single biconcave parabolic refractive lens array, Sci. Rep. 9 (2019), https://doi.org/10.1038/s41598-019-50869-8.
[19] L. Xu, X. Zeng, Z. Huang, W. Li, H. Zhang, Low-dose chest X-ray image super-resolution using generativeadversarial nets with spectral normalization, Biomed. Signal Process Contr. 55 (2020), 101600.
[20] M. Elad, A. Feuer, Restoration of a single superresolution image from several blurred, noisy, and undersampled measured images, IEEE Transsanctions on Image Processing 6 (1997) 1646–1658.
[21] N. Nguyen, P. Milanfar, G. Golub, Efficient generalized cross-validation with applications to parametric image restoration and resolution enhancement, IEEE Transsanctions on Image Processing 10 (2001) 1299–1308.
[22] S.C. Park, M.K. Park, M.G. Kang, Super-resolution image reconstruction: a technical overview, IEEE Signal Process. Mag. (2003) 21–36.
[23] M. Irani, S. Peleg, Improving resolution by image registration, CVGIP Graph. Models Image Process. 53 (1991) 231–239.
[24] S. Farsiu, M.D. Robinson, M. Elad, P. Milanfar, Fast and robust multiframe super resolution, IEEE Transsanctions on Image Processing 13 (2004) 1327–1344.
[25] S. Baker, T. Kanade, Limits on super-resolution and how to break them, IEEE Trans. Pattern Anal. Mach. Intell. 24 (2002) 1167–1183.
[26] Z. Lin, H. Shum, Fundamental limits of reconstruction-based superresolution algorithms under local translation, IEEE Trans. Pattern Anal. Mach. Intell. 26 (2004) 83–97.
[27] W.T. Freeman, E.C. Pasztor, O.T. Carmichael, Learning low-level vision, Int. J. Comput. Vis. 40 (2000) 25–47.
[28] W.T. Freeman, T.R. Jones, E.C. Pasztor, Example-based super-resolution, IEEE Computer Graphics and Applications 22 (2002) 56–65.
[29] R. Fattal, Image upsampling via imposed edge statistics, ACM Trans. Graph. 26 (2007), 95-1-8.
[30] J. Sun, J. Sun, Z. Xu, H. Shum, Image super-resolution using gradient profile prior, in: 2008 IEEE Conference on Computer Vision and Pattern Recognition, 2008, pp. 23–28.
[31] D. Glasner, S. Bagon, M. Irani, Super-resolution from a single image, in: 2009 IEEE 12th International Conference on Computer Vision, 2009, https://doi.org/10.1109/ICCV.2009.5459271.
[32] J. Yang, Z. Wang, Z. Lin, S. Cohen, T. Huang, Coupled dictionary training for image super-resolution, IEEE Transsanctions on Image Processing 21 (2012) 3467–3478.
[33] J. Yang, Z. Lin, S. Cohen, Fast image super-resolution based on in-place example regression, in: 2013 IEEE Conference on Computer Vision and Pattern Recognition, CVPR, 2013, pp. 1059–1066.
[34] J. Huang, A. Singh, N. Ahuja, Single image super-resolution from transformed self-exemplars, in: 2015 IEEE Conference on Computer Vision and Pattern Recognition, CVPR, 2015, pp. 5197–5206.
[35] C. Dong, C.C. Loy, K. He, X. Tang, Image super-resolution using deep convolutional networks, IEEE Trans. Pattern Anal. Mach. Intell. 38 (2016) 295–307.
[36] J. Kim, J.K. Lee, K.M. Lee, Accurate image super-resolution using very deep convolutional networks, in: 2016 IEEE Conference on Computer Vision and Pattern Recognition, CVPR, 2016, pp. 1646–1654.
[37] J. Kim, J.K. Lee, K.M. Lee, Deeply-recursive convolutional network for image super-resolution, in: 2016 IEEE Conference on Computer Vision and Pattern Recognition, CVPR, 2016, pp. 1637–1645.
[38] G. Huang, Z. Liu, L.V.D. Maaten, K.Q. Weinberger, Densely connected convolutional networks, in: 2017 IEEE Conference on Computer Vision and Pattern Recognition, CVPR, 2017, pp. 2261–2269.
[39] T. Tong, G. Li, X. Liu, Q. Gao, Image super-resolution using dense skip connections, in: 2017 IEEE International Conference on Computer Vision, CVPR, 2017, pp. 4809–4817.
[40] Y. Zhang, Y. Tian, Y. Kong, B. Zhong, Y. Fu, Residual dense network for image super-resolution, in: 2018 IEEE/CVF Conference on Computer Vision and Pattern Recognition, 2018, pp. 2472–2481.
[41] M. Koutalonis, H. Delis, G. Spyrou, L. Costaridou, G. Tzanakos, G. Panayiotakis, Contrast-to-noise ratio in magnification mammography: a Monte Carlo study, Phys. Med. Biol. 52 (2007) 3185–3199.
[42] O.M. Rijal, H. Ebrahimian, N.M. Noor, Determining features for discriminating PTB and normal lungs using phase congruency model, in: Proceedings of 2012 IEEE-EMBS International Conference on Biomedical and Health Informatics, BHI 2012, 2012, pp. 341–344.
[43] L. Yu, X. Zhang, Y. Chu, Super-resolution reconstruction algorithm for infrared image with double regular items based on sub-pixel convolution, Appl. Sci. 10 (2020), https://doi.org/10.3390/app10031109.
[44] J.T. Dobbins III, E. Samei, N.T. Ranger, Y. Chen, Intercomparison of methods for image quality characterization. II. Noise power spectrum, Med. Phys. 33 (2006) 1466–1475.
[45] S. Ioffe, C. Szegedy, Batch Normalization: Accelerating Deep Network Training by Reducing Internal Covariate Shift, arXiv preprint (2015) arXiv:1502.03167.
[46] D. P. Kingma, J. Ba, Adam: a Method for Stochastic Optimization, arXiv preprint (2014) arXiv:1412.6980.
[47] S.Y. Chun, J.A. Fessler, Y.K. Dewaraja, Post-reconstruction non-local means filtering methods using CT side information for quantitative SPECT, Phys. Med. Biol. 58 (2013) 6225–6240.